Mapping and Removing the Ventricular Far Field Component in Unipolar Atrial Electrograms

Daniel Frisch, *Member, IEEE*, Tobias G Oesterlein, Laura A Unger, *Member, IEEE*, Gustavo Lenis, Reza Wakili, Claus Schmitt, Armin Luik, Olaf Dössel, *Senior Member, IEEE*, Axel Loewe*, *Member, IEEE*

Abstract*—*Objective: **Unipolar intracardiac electrograms (uEGMs) measured inside the atria during electro-anatomic mapping contain diagnostic information about cardiac excitation and tissue properties. The ventricular far field (VFF) caused by ventricular depolarization compromises these signals. Current signal processing techniques require several seconds of local uEGMs to remove the VFF component and thus prolong the clinical mapping procedure. We developed an approach to remove the VFF component using data obtained during initial anatomy acquisition. *Methods:* We developed two models which can approximate the spatio-temporal distribution of the VFF component based on acquired EGM data: Polynomial fit, and dipole fit. Both were benchmarked based on simulated cardiac excitation in two models of the human heart and applied to clinical data. *Results:* VFF data acquired in one atrium were used to estimate model parameters. Under realistic noise conditions, a dipole model approximated the VFF with a median deviation of 0.029 mV, yielding a median VFF attenuation of 142. In a different setup, only VFF data acquired at distances of more than 5 mm to the atrial endocardium were used to estimate the model parameters. The VFF component was then extrapolated for a layer of 5 mm thickness lining the endocardial tissue. A median deviation of 0.082 mV (median VFF attenuation of 49x) was achieved under realistic noise conditions. *Conclusion:* It is feasible to model the VFF component in a personalized way and effectively remove it from uEGMs. *Significance:* Application of our novel, simple and computationally inexpensive methods allows immediate diagnostic assessment of uEGM data without prolonging data acquisition.**

Manuscript received mmmmmmm dd, 2019; revised mmmmmmm dd, yyyy and mmmmmmm dd, yyyy; accepted mmmmmmm dd, yyyy. Date of current version March 05, 2019.

The research leading to these results has received funding from the German Research Foundation (DFG) under grant DO637/14-1, DO637/22-3, and DO637/23-1. We gratefully acknowledge financial support by Deutsche Forschungsgemeinschaft (DFG) through CRC 1173 and by the Ministerium für Wissenschaft, Forschung und Kunst Baden-Württemberg through the Research Seed Capital (RiSC) program. *Asterisk indicates corresponding author. D. Frisch and T. G. Oesterlein contributed equally to this work.* Patents addressing the proposed analysis technique were filed by Karlsruhe Institute of Technology (KIT), Karlsruhe [1]. D. Frisch was with the Institute of Biomedical Engineering (IBT), Karlsruhe Institute of Technology (KIT), Karlsruhe, Germany and is now with the Institute for Anthropomatics and Robotics, Chair for Intelligent Sensor-Actuator-Systems (ISAS) at KIT. L. A. Unger, G. Lenis, O. Dössel, and A. Loewe are with the Institute of Biomedical Engineering (IBT), Karlsruhe Institute of Technology (KIT), Karlsruhe, Germany. (e-mail: publications@ibt.kit.edu) T. G. Oesterlein was with the Institute of Biomedical Engineering (IBT), Karlsruhe Institute of Technology (KIT), Karlsruhe, Germany and is now with Boston Scientific, Malborough, MA, USA. R. Wakili is with the West-German Heart and Vascular Center, Essen, Germany. C. Schmitt and A. Luik are with Städtisches Klinikum Karlsruhe, Karlsruhe, Germany.

***Index Terms*—Electroanatomic mapping, intracardiac electrogram, high-density mapping, ventricular far field**

I. Introduction

INTRACARDIAC mapping has become a cornerstone of cardiac arrhythmia diagnostic procedures. During electrophysiological studies, catheters equipped with electrodes allow to acquire electrograms (EGMs) at the endocardial surface. Diagnostic information regarding the arrhythmia mechanism and the state of the tissue is derived from the EGMs to guide therapy. Intracardiac electrodes record the local electric potential with respect to a reference electrode. Subtracting these so called unipolar EGMs (uEGMs) of two adjacent electrodes yields bipolar EGMs (bEGMs) with reduced common mode components [2]. Analysis of uEGMs and bEGMs allows to understand the mechanisms of atrial arrhythmias and to develop patient-specific treatment strategies [3]. While currently bEGMs are most widely used, our method enables full utilization of the complementary uEGMs.

Our main assumption is that amplitude, width, and morphology of uEGMs for a given cardiac activation sequence depend only on the electrode location, reflecting the *electric potential*, which is a scalar field. Every uEGM that has been recorded close enough to the atrial wall can be incorporated in the processing, as it directly represents the local atrial activity related to that one electrode. Additive noise components that appear on multiple channels simultaneously, are cancelled in bEGMs by the subtraction operation resulting in a better signal-to-noise ratio than unprocessed uEGMs. This simple noise reduction technique, however, comes at a price. Basically, bEGMs measure the *directional derivative* $\nabla\Phi$ of the electric potential Φ at point $\boldsymbol{x}_0$, scaled by the electrode distance $||\boldsymbol{d}||$,

$$\text{bEGM}(\boldsymbol{x}_0) = \Phi(\boldsymbol{x}_0 + \tfrac{1}{2}\boldsymbol{d}) - \Phi(\boldsymbol{x}_0 - \tfrac{1}{2}\boldsymbol{d}) \approx (\nabla\Phi)(\boldsymbol{x}_0) \cdot \boldsymbol{d}\ ,$$

where $\boldsymbol{d}$ is the vector connecting the two electrodes of the bEGM channel. Therefore, the signal morphology and amplitude of bEGMs depends markedly on alignment of wavefront direction and catheter orientation [2], [4]. As a consequence, morphological analyses, for example transmural lesion detection [5], are always more complicated when based on bEGMs. Even activation time measurement with bEMGs requires fairly parallel orientation of wavefront direction and electrodes, and electrode spacing should not exceed 2 mm [6]. In addition, bEGMs by definition contain less (and less localized) signal channels than uEGMs because from a row of n electrodes and their n corresponding uEGMs, only $(n-1)$

bEMGs are suitable for analysis. On some catheters, electrodes are arranged in pairs to achieve very small inter-electrode-spacings and hence maximize spatial resolution. In this case however, only $n/2$ bEGMs are produced. In summary, we conclude that uEMGs leverage more signal channels that are more localized and easier to interpret than bEGMs. We propose a method that cancels unwanted components from uEGMs without the negative side effects imposed by using bEGMs.

Besides baseline wander [7], [8] and high-frequency noise [9] that can be removed by linear time-invariant (LTI) filtering techniques, the major component compromising atrial uEGMs is the so-called ventricular far field (VFF) [2]. The VFF is caused by depolarization and repolarization of the ventricles and leads to a signal which is often larger than the desired atrial signal [2], [10]. As the VFF overlaps with the desired atrial activity in both time and frequency domain [11], it cannot be removed by standard filtering techniques. Instead, clinical practice focuses on bEGMs. While reducing the VFF component, bEGMs can compromise diagnostically relevant information like the local activation time (LAT), peak-to-peak voltage or signal morphology. The latter two additionally depend on catheter orientation [2], [3], [6], [12]. Moreover, the VFF is often still visible in bEMGs, especially if the electrodes are aligned perpendicular to the atrial wavefront direction (small atrial signal) but oriented in parallel with the direction towards the ventricles (in line with the VFF gradient, high ventricular signal).

A. State of the Art

The easiest way to remove all VFF is simply blanking all uEGMs around R peaks. However, the resulting fragmented signals are much harder to interpret for both humans and algorithms, and a considerable part of the available information gets lost. For example, think of features that compare successive basic cycle lengths of atrial activations.

Several signal processing techniques already exist that are able to separate undesired VFF from desired atrial activity in surface electrocardiograms (ECGs) [13], [14], [15] and uEGMs [10], [11], [16], [17]. Based on a number of recorded ventricular activation events, they learn the local signal course of the VFF. Average beat subtraction as well as template matching with subsequent subtraction create a VFF template by aligning and averaging the ventricular events. Alternatively, Principle Component Analysis (PCA) can be applied to identify the common, ventricular parts, and allows to accurately control the degree of cancellation. These methods require atrial and ventricular activity to be statistically independent. Periodic Component Analysis (πCA) additionally exploits the periodicity of the atrial, wanted signal, and thus works even in cases where atrial and ventricular activations are coupled to some degree, like in atrial flutter (AFlut) [17]. Other approaches aim to reproduce the VFF by filtering a reference channel like ECG II with an LTI filter. All of these methods require a training phase containing *multiple* ventricular activations, ranging from 5–60 s, during which the catheter must be held still. This training has to be repeated after each change of catheter position. To obtain state of the art map densities (more than 15000 points on average [3]), this prolongs the procedure by more than one hour, even if simultaneous wall contact of 20 electrodes per mapping position is assumed.

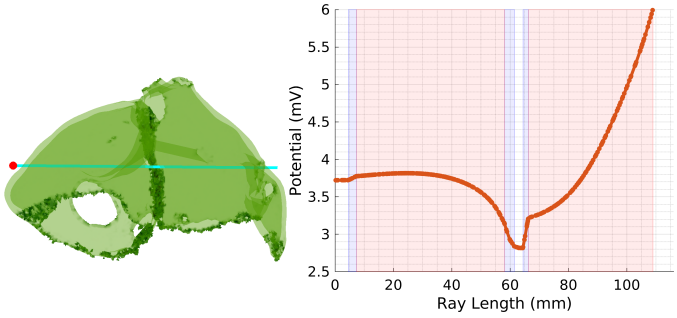

(a) Ray through atrial geometry, anterior view.

(b) VFF at 164 ms.

Fig. 1. Simulated extracellular potential along a trace through both atria, in SimB at 164 ms. Red dot in (a) denotes the 0 mm point. Blue background in (b) denotes atrial myocardium and red background denotes atrial cavities; the white background between the atria (septum) and around the atria is also filled with blood in the simulation. The reference potential is arbitrary.

We sought to develop a method for removing the VFF instantaneously and without the need for repeated training.

B. Key Idea

Based on anatomical, physiological and physical considerations, we hypothesized that the spatial course of the VFF is smooth within an atrial cavity (see Fig. 1b), and that one can parameterize a suitable spatio-temporal model using routine mapping data to approximate and, if necessary, extrapolate the VFF component. To this end, we exploit the ability of modern electroanatomical mapping systems to accurately track electrode locations while recording uEGMs.

We assume that the spatio-temporal VFF template looks the same again anytime the catheter re-visits the same location. Furthermore, the VFF template at any point in the atria may be interpolated by the VFF templates generated at adjacent points. When a sufficiently dense map of VFF templates at many points inside the atria is available, the template at any point can be obtained without further learning. We propose to generate a smooth spatial model of the VFF potential for every time step relative to the R peak. To our knowledge, such spatial models of the VFF have not been proposed before.

The method does not make any assumptions about the atrial rhythm or its statistical independence from the ventricular rhythm, and hence works for all kinds of rhythms including atrial fibrillation (AFib) and AFlut likewise. The only requirements are accurate electrode tracking, and a recurring type of ventricular depolarization, i.e., no ventricular extrasystoles. Furthermore, it is important that the atrial component is cancelled out during VFF model generation. This can be achieved by temporal windowing in sinus rhythm or recording far enough from the atrial wall in AFlut.

Two spatial modeling approaches are assessed in the following on both simulated and human clinical data, demonstrating that this concept can strongly improve the quality of uEGMs.

II. Methods

We evaluated the capability of different spatial models to approximate the simulated VFF inside the atria. We applied rather generic polynomial models of variable degree, and a more physically substantiated model with dipole current sources in the ventricles. In either case, each time step sustains its own system model, i.e., the estimation of the model's parameters was independent of the VFF at previous time steps. The best-performing models were then applied to clinical data.

The cardiac electrophysiology of a single heart beat was simulated for two anatomical models, which we will call SimA and SimB. The extracellular electrical potential due to the cardiac excitation spread was calculated using a bidomain approach [18] at each vertex of the geometry and served as the ground truth data to estimate the parameters of the spatial model at each individual time step. In order to get a high-density spatial map of the actual VFF for clinical data as well, we used EGM data from multiple heart beats and aligned them to the R peaks in the simultaneously recorded surface ECG.

A. Polynomial Model

Deriving a bEGM from two uEGMs has been shown to reduce the ventricular component [2]. In the bEGM context, VFF is assumed to be spatially constant, i.e., a polynomial of 0^{th} degree, within the range of the two contributing electrodes. Thus, we hypothesized that the spatial course of the potential could as well be approximated within a larger range when using a polynomial model of higher degree. In fact, Taylor's theorem states that any N_d times differentiable function can be approximated by a polynomial of degree N_d, and the electric potential actually is indefinitely differentiable inside a source-free homogeneous conductor like the blood-filled atrial cavities. In Fig. 1b, one can inspect the smoothness inside the cavities, as well as the non-smooth behavior at boundaries like the septum.

Mathematically, any polynomial of degree N_d is a linear combination of monomials up to degree N_d. Therefore, we set up a measurement model matrix $\mathbf{X}$ that contains the values of these monomials at positions $\boldsymbol{r}_m = \begin{bmatrix} x_m & y_m & z_m \end{bmatrix}^\top$, $m \in \{1, 2, ..., M\}$, $\boldsymbol{x}^\top$ is $\boldsymbol{x}$ transposed. For example, the model matrix $\mathbf{X}$ for a 2^{nd} order polynomial, i.e., $N_d = 2$, is

$$\mathbf{X} = \begin{pmatrix} 1 & x_1 & y_1 & z_1 & x_1y_1 & x_1z_1 & y_1z_1 & x_1^2 & y_1^2 & z_1^2 \\ 1 & x_2 & y_2 & z_2 & x_2y_2 & x_2z_2 & y_2z_2 & x_2^2 & y_2^2 & z_2^2 \\ & & & & & \dots & & & & \\ 1 & x_M & y_M & z_M & x_My_M & x_Mz_M & y_Mz_M & x_M^2 & y_M^2 & z_M^2 \end{pmatrix} . \tag{1}$$

VFF measurements $\Phi_{k,m}$, obtained at location $\boldsymbol{r}_m$ and time k (k relative to R peak), are put into measurement vector $\boldsymbol{\Phi}_k = \begin{bmatrix} \Phi_{k,1} & \dots & \Phi_{k,M} \end{bmatrix}^\top$. Expressing the VFF as a spatial polynomial then results in

$$\boldsymbol{\Phi}_k = \mathbf{X}\,\boldsymbol{c}_k \ , \tag{2}$$

where $\boldsymbol{c}_k$ contains the weighting factors of the individual monomials making up the polynomial. Note that this model is nonlinear in $\boldsymbol{r}$, but linear in $\boldsymbol{c}_k$. Therefore, the standard least squares solution of $\boldsymbol{c}_k$ can be obtained using the pseudoinverse of $\mathbf{X}$. Having $\boldsymbol{c}_k$, the VFF Φ_k can be easily estimated at any point $\boldsymbol{r}$.

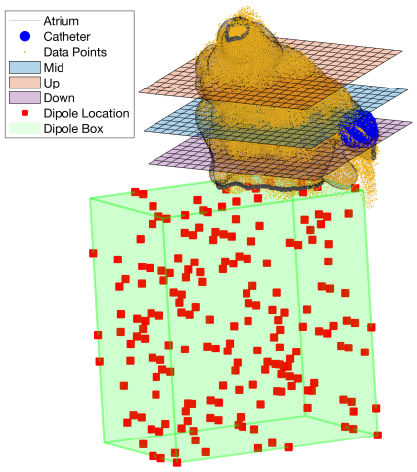

Fig. 2. Exemplary distribution of assumed ventricular dipole locations (red) in the clinical data set. One exemplary catheter position is shown in blue. The $1486 \cdot 64 = 95104$ collected VFF data points in the atrium are indicated as small orange dots. In addition, three partitioning planes (Mid, Up, Down) are shown that were used for a variant of the polynomial model employing spatially separated sub-models.

The total number of parameters N_p in a polynomial model of degree N_d in $\mathbb{R}^3$ is given by the number of all possible monomials of three variables with a degree up to N_d,

$$N_p = \sum_{k=0}^{N_d} \binom{3+k-1}{k} = \frac{1}{6}(N_d+1)(N_d+2)(N_d+3) \ . \tag{3}$$

B. Dipole Model

The electrical potential at the body surface and within the body is caused by electric dipole current sources, or impressed currents, originating from the depolarization and repolarization of cardiac tissue. This motivates a biophysical dipole model as alternative approach. A detailed reconstruction of the source distribution based on measured potentials is subject of the inverse problem of electrocardiography [19]. In this work, however, we hypothesized that a less detailed reconstruction is sufficient for the formulation of a linear model that can appropriately describe the VFF just within the atrium that is currently being mapped.

Every possible distribution of impressed currents can be expressed by the current dipole density $\boldsymbol{J}_k(\boldsymbol{r})$, which is a vector field. In a homogeneous volume conductor of infinite size, the potential Φ_k at measurement point $\boldsymbol{r}_m$ is given by the volume integral

$$\Phi_k(\boldsymbol{r}_m) = \frac{1}{4\pi\kappa} \iiint \boldsymbol{J}_k(\boldsymbol{r}') \cdot \frac{(\boldsymbol{r}_m - \boldsymbol{r}')}{|\boldsymbol{r}_m - \boldsymbol{r}'|^3}\, \mathrm{d}v' \ ,$$

where κ denotes the conductivity of the material, v' the infinitesimal volume element for integration, $\boldsymbol{r}'$ the integration variable, and the reference point is located in infinity. For discrete dipole locations $\boldsymbol{r}'_p$, this integral turns into a sum, and the *lead field matrix* is the according linear model that

maps magnitude and direction of the individual electric current dipoles $\boldsymbol{J}(\boldsymbol{r}'_p)$ to the electric potential $\Phi_k(\boldsymbol{r}_m)$.

For a single current dipole located at $\boldsymbol{r}_p$ and one electrode at $\boldsymbol{r}_m$, where the reference potential is located at $\boldsymbol{r}_0$, the lead field has only one row $\boldsymbol{x}_m^\top$

$$\boldsymbol{x}_m^\top = \frac{1}{4\pi\kappa}\left[\frac{(\boldsymbol{r}_m-\boldsymbol{r}_p)^\top}{|\boldsymbol{r}_m-\boldsymbol{r}_p|^3} - \frac{(\boldsymbol{r}_0-\boldsymbol{r}_p)^\top}{|\boldsymbol{r}_0-\boldsymbol{r}_p|^3}\right] . \tag{4}$$

The full matrix $\mathbf{X}$ for M electrodes will contain M such rows $\mathbf{X} = [\boldsymbol{x}_1,\ldots,\boldsymbol{x}_M]^\top$. More dipoles can be added by adding additional columns to $\mathbf{X}$ and entries to $\boldsymbol{c}_k$. Finally, the measurement model is

$$\boldsymbol{\Phi}_k = \mathbf{X}\,\boldsymbol{c}_k \ . \tag{5}$$

The parameters $\boldsymbol{c}_k$ of this model are the impressed currents along the three spatial directions, $\boldsymbol{J}_k(\boldsymbol{r}_p) = \begin{bmatrix}J_{k,p,x} & J_{k,p,y} & J_{k,p,z}\end{bmatrix}^\top$. Instead of choosing a fixed reference point $\boldsymbol{r}_0$, one can also *estimate* the reference potential by adding a column of ones to $\mathbf{X}$, just like the first column in (1), and one more parameter to $\boldsymbol{c}_k$. In total, the number of parameters N_p of this model with N_d spatially fixed dipoles is

$$N_p = N_d \cdot 3 + 1 \ . \tag{6}$$

Again, this model is nonlinear in $\boldsymbol{r}_m$ but linear in $\boldsymbol{c}_k$ – as long as the dipole locations $\boldsymbol{r}_p$ are fixed. In our simulations, VFF dipoles were placed equally distributed in the simulated ventricular myocardium, or into the convex hull of the ventricles, respectively. For clinical data, the ventricular anatomy was not available, and a $10\times10\times10$ dipole grid was created inside a cuboid of size $104\,\mathrm{mm}\times77\,\mathrm{mm}\times115\,\mathrm{mm}$ inferior to the atria. In any case, an equally distributed subset of these reference locations was generated to obtain models of arbitrary order for comparison. An example for the placement of dipoles in a clinical data set is depicted in Fig. 2.

C. Spatial Separation of Models

More detailed models result from increasing the model complexity by either using a polynomial model of higher degree or a dipole model with more dipoles. Another option is to spatially separate the atria into multiple regions, which are each represented by a different model and parameter set. It may be beneficial to identify the optimal combination of model complexity and spatial separation.

Specifically, besides considering the left atrium (LA) and the right atrium (RA) as distinct model environments, the atrial space was separated by planes parallel to the valve plane (see Fig. 2) both for the polynomial and the dipole model in order to investigate possible improvements in approximation quality.

D. VFF Component Removal Workflow

In this section, we will recapitulate the necessary steps to apply our VFF removal technique to any intracardiac recording. You can also find a corresponding flow chart in Supplemental Fig. 7.

First, we need a recording of the recurring, pure VFF signal inside the atria. Therefore, the atria are mapped, preferably while not fibrillating – for instance during initial anatomy acquisition. R peak detection is applied based on the ECG [20], and a window of ventricular activity is extracted that extends for example from 50 ms before to 210 ms after the R peak to cover the QRS complex. This temporal window can be adapted to the individual patient to cover QRS complex and optionally T wave. All recorded segments are aligned to the R peak and stored together with the corresponding electrode location. When using the IntellaMap Orion (Boston Scientific, Marlborough, MA, USA) catheter, we get the VFF at 64 locations with every ventricular contraction. In cases of atrial activity taking place synchronous to VFF already during acquisition phase, like in atrial reentrant tachycardia or AFib, one could still use electrograms where the VFF dominates (e.g. $>5\,\mathrm{mm}$ distance to the endocardium towards the center of the chamber). We will see that the VFF can then be extrapolated to some degree.

The acquired data composes a three-dimensional map with the measured VFF potential $\hat{\boldsymbol{\Phi}}_k$ at thousands of points inside the atrium for each time step relative to the R peak. Now we fit the model to these data by calculating the parameter vector $\hat{\boldsymbol{c}}_k$ for each time step using the pseudoinverse of the model matrix $\mathbf{X}$.

Later, during the actual electrophysiological study, while the atria present with an arbitrary rhythm such as AFib or AFlut, we perform on-the-fly R peak detection, take the parameter vector $\boldsymbol{c}_k$ of the respective time step relative to the detected R peak, and calculate the expected VFF at the current catheter locations using (1) and (2) or (4) and (5). After subtracting the VFF from the uEGMs, we ideally obtain the pure atrial signal. Fig. 3 gives a simulated example of VFF cancellation in a window of simulated ventricular activity.

E. Simulations

Both methods were evaluated using simulated data first, giving the advantage that the ground truth can be obtained [21], [22]. Two different cardiac anatomies were used. The first one was obtained from a segmentation of the Visible Man cryosection data set [23], [24], and used to simulate ventricular excitation and the resulting potential in the entire thorax. It will be referred to as SimA. The second anatomy was derived from MRI data of a healthy 26-year-old male [25] and used to simulate ventricular as well as atrial excitation. It will be referred to as SimB in the following. See Supplemental Fig. 1 – 3 for details on the geometrical setup of SimB. This cardiac model was immersed in blood, which filled the cavities and surrounded the heart by 3 to 6 mm. Both anatomical data sets were augmented with rule-based fiber orientation [26], [27]. Atrial excitation was triggered from the junction of the right atrial appendage with the superior vena cava [25], and membrane kinetics were represented by heterogeneous variants of the Courtemanche *et al.* model [28], [29]. The ventricular myocardium was stimulated by a profile mimicking Purkinje activation [30]. Membrane kinetics were represented by the ten Tusscher-Panfilov model [31]. Intracellular conductivities were adapted to obtain a realistic activation profile. Excitation propagation simulations were conducted with the cardiac

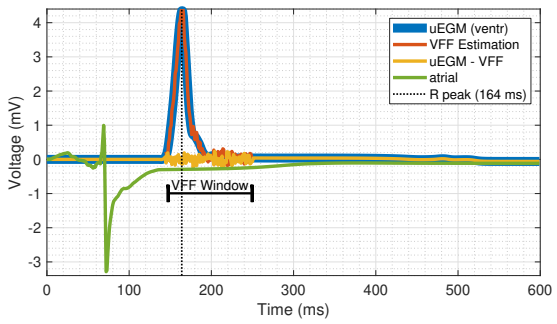

Fig. 3. Extracellular potential in the LA of SimB at one exemplary vertex near the septum in 30 mm distance to the valve plane and in 1 mm distance to the atrial wall. The blue signal represents the virtually measured uEGM consisting of ventricular activity only. A dipole model with 10 ventricular dipoles in the convex hull of both ventricles was trained based on all uEGMs, which were distorted by additive white Gaussian noise ($\sigma = 1\,\mathrm{mV}$). The rectangular VFF window includes the time interval between 145 ms and 250 ms around the R peak at 164 ms. The red line segment represents the VFF model evaluated at the selected point, i.e., our proposed model's approximation of the blue line. The orange line shows the VFF-cleared signal resulting when the VFF approximation is subtracted from the measured signal. Note that the VFF window could easily be extended to the right in order to cover repolarization effects as well. The simulated atrial uEGM is shown in green. Its repolarization clearly overlaps with the VFF but this would be removed by highpass filtering in clinical setups.

simulation framework acCELLerate [18], [32] with a finite element scheme solving the bidomain formulation and yielding a realistic EGM and ECG [30]. The spread of excitation in the atria and ventricles is shown in Supplemental Fig. 4 and 5.

In the geometry of SimA, 97 % of the tetrahedral edges defining atrial myocardium measured between 1 and 2 mm in length. The tetrahedra inside the cavities were considerably larger with edge lengths of up to 5.6 mm. Since the extracellular potential was only simulated at the vertices, the spatial resolution limited the amount of available data. The cavities had 9163 and 21059 vertices in LA and RA, respectively, with a subset of 125 and 836 vertices being located in more than 5 mm distance to the endocardium. The mesh of SimB, in contrast, had a uniformly high spatial resolution with edge lengths between 0.9 and 2.1 mm for 99 % of the tetrahedra, (see also Supplemental Fig. 2). 37185 and 65983 vertices were in the LA and RA cavities, respectively, with a subset of 11739 and 30328 vertices being located in more than 5 mm distance to the endocardium.

Simulation of one heart beat was performed to obtain continuous uEGM data for all vertices in the atrial cavities. For SimA, only the ventricular activity was simulated. For SimB, uEGMs based on ventricular activities only, atrial activities only, and the combined activities were obtained separately. Fig. 3 shows the simulated signal at one vertex in SimB.

F. Clinical Data

A 67 year old female patient underwent catheter ablation for persistent AFib at Städtisches Klinikum Karlsruhe (Karlsruhe, Germany), using the electroanatomic mapping system Rhythmia HDx (Boston Scientific, Marlborough, MA, USA). Written informed consent was obtained for the procedure and data analysis. The biatrial anatomy as well as voltage and activation time information were obtained during paced rhythm (see Supplemental Fig. 8 – 10 for details on the clinical mapping procedure). For LA and RA, anatomy acquisition took 1211 s and 924 s, 1486 and 1170 R peaks were detected, and the anatomical surfaces consisted of 11921 and 11914 triangles, respectively. The data recorded during initial anatomy acquisition were also used for generating the VFF model.

In agreement with the study protocol, additional mapping data were acquired. Subsequently, AFib was induced and the recordings continued. Approximately one hour after anatomy acquisition had been completed, the Orion catheter was inserted to record data at specific locations in LA. The offset of one hour resulted from the study protocol and allowed us to assess temporal stability of our approach. Following the procedure, atrial anatomies, ECGs, uEGMs, and electrode position traces were exported for retrospective analysis.

In a first step, QRS complexes were annotated in the ECG using a wavelet-based approach [7], [20]. A time window of about -50 to +210 ms was set around the R peaks by visual inspection for this data set, to ensure that atrial excitation had completed before (see Supplemental Fig. 10). The uEGMs and electrode positions were synchronized for this window (see Supplemental Fig. 11). Standard filtering was performed internally by the electroanatomical mapping system including a highpass and a lowpass filter with cutoff frequencies of 1 Hz and 300 Hz, respectively, as well as the rejection of the power line frequency. No additional filtering was applied prior to VFF potential field model estimation. For better visualization after VFF cancellation, we optionally apply 2^{nd} order Butterworth filtering with cutoff frequencies at 0.5 and 300 Hz in combination with Gaussian notch filtering (width 1 Hz) to remove some dominant noise peaks $\geq$160 Hz from the spectrum.

We assume that R peaks are detected correctly, that the spatio-temporal course of the VFF is repetitive for all ventricular beats, and that the mapping system provides accurate and consistent electrode locations.

G. Evaluation

The spatial derivative of the VFF potential, i.e., the electric field was computed in SimB to assess its smoothness and gradient steepness, see Fig. 4 and Supplemental Fig. 6. In the clinical data, a 3D Gaussian filter with $\sigma = 2\,\mathrm{mm}$ was applied before calculating the gradient to suppress noise. Table I summarizes absolute gradient values and their dependency on the distance to the valve plane. See Supplemental Fig. 14 and 15 for details.

To assess the capability of polynomial and dipole methods to approximate and extrapolate the VFF, least-squares estimations of (2) and (5) were performed, and the median residual voltage was computed within a 5 mm layer of blood lining the endocardium. VFF-free uEGMs of atrial activity within the mentioned layer carry the diagnostically relevant information and are of great interest during electrophysiological studies.

Model performance was compared for different variants of spatial partitioning (see Fig. 2) and varying numbers of model parameters. The number N_p of free model parameters (3) or

TABLE I
MEDIAN SPATIAL GRADIENT IN $\mathrm{mV/mm}$ AT THE TIME OF THE R PEAK WITHIN 10 mm THICK SLICES PARALLEL TO THE VALVE PLANE. CLINICAL DATA WERE SMOOTHED WITH A 3D GAUSSIAN FILTER ($\sigma = 2\,\mathrm{mm}$) BEFORE CALCULATING THE GRADIENT.

Distance to valve plane	SimB	Clinical
0 mm	0.41	0.18
10 mm	0.17	0.1
20 mm	0.086	0.078
30 mm	0.048	0.055
40 mm	0.031	0.033
50 mm	0.024	0.032
60 mm	0.015	0.027
70 mm	–	0.025

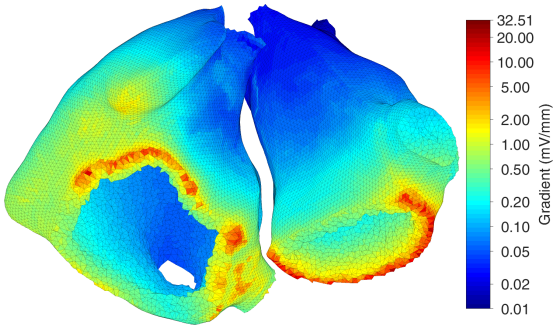

Fig. 4. The absolute value of the spatial gradient of the VFF of SimB was calculated for a layer of 5 mm thickness lining the endocardium. The maximum absolute gradient over time is color coded logarithmically for each tetrahedron.

(6) was used as abscissa to allow for a common benchmarking scheme for both methods.

III. RESULTS

A. Spatial Course of VFF Potential

The simulated ventricular excitations allowed to inspect the VFF potential inside the atrial chambers. VFF potential along a ray through both atria of SimB is shown in Fig. 1. Different conductivities in blood and tissue cause discontinuities in the electric field at the septum. This motivated the generation of independent models for both atria. The absolute value of the spatial gradient decreased with increasing distance to the valve plane. The maximum value in the LA of SimB was about 1–2 mV/mm with a median of 0.1 mV/mm (see Fig. 4 and Supplemental Fig. 6).

Clinically measured potentials inside the LA are shown in Fig. 5. A video of the distribution's time course and a visualization of the potential on a ray from roof to mitral valve, is provided as a supplement and explained in Supplemental Fig. 22.

B. Approximation of the Measured Field

A visual comparison between the simulated VFF and the dipole approximation is presented in Supplemental Fig. 21 and the corresponding video.

In order to quantify how well models can approximate the field distribution in general, all vertices inside the atria were used to parametrize, i.e., train, the models initially. In SimB,

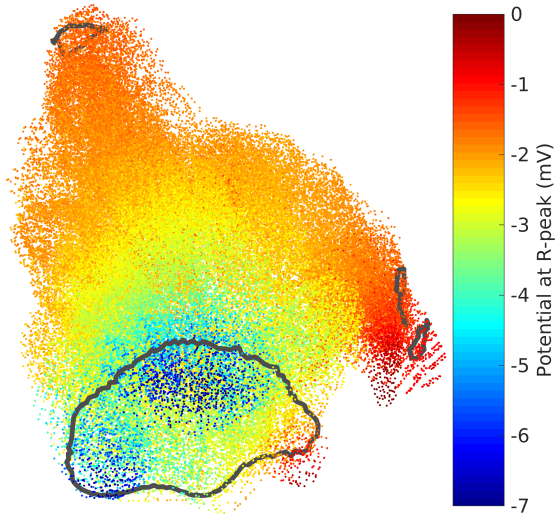

Fig. 5. Clinically measured extracellular potential at 95104 sites in LA at the moment of the R peak. Note the continuous spatial course of the VFF and its dependence on the distance to the valve plane. The median spatial gradient was 0.054 mV/mm. Pulmonary vein ostia and mitral valve opening are visualized as thick grey lines for orientation.

additive Gaussian noise ($\sigma = 1\,\mathrm{mV}$) was also imposed on the uEGMs before training, which is a rather pessimistic choice [33, Fig. 4]. The quality of fit was assessed by evaluating the 5 mm intraatrial layer close to the endocardial wall. Fig. 6a and 6b show the performance of VFF approximation in SimA and SimB, respectively, for different models and all contemplated numbers of model parameters.

Unsurprisingly, the approximation quality initially got better with increasing numbers of parameters for all methods. However, beyond 10^3 parameters, the performance of the polynomial methods collapsed, probably due to numerical issues. Furthermore, the performance of polynomial models decreased starting from 100 parameters when noise was added to the signals. The dipole models did not show this undesirable behavior. A practical choice could be a dipole model with 42 dipoles and 127 parameters (6), yielding a median deviation of 0.029 mV (IQR 0.013–0.064 mV). The median VFF suppression factor was 142 (IQR 65.2–322).

C. Extrapolation of the Measured Field

As it may not be possible to map the VFF potential in the entire atrial chamber, it is important to know whether the proposed methods can extrapolate the VFF distribution. Therefore, we trained the model by considering only data from vertices with more than 5 mm distance to the endocardium, and afterwards estimated the VFF distribution at the other locations, i.e., with less than 5 mm distance to the endocardium. Again, training data were distorted by Gaussian noise with $\sigma = 1\,\mathrm{mV}$.

The resulting performance for SimB is shown in Fig. 6c. In contrast to Fig. 6b, the dipole model performance also deteriorated for more than 40 parameters. Thus, 12 dipoles with 37 parameters appear to be the best model in this case, yielding a median deviation of 0.082 mV (IQR 0.033–0.19 mV). The median VFF suppression factor was 49 (IQR 21–124).

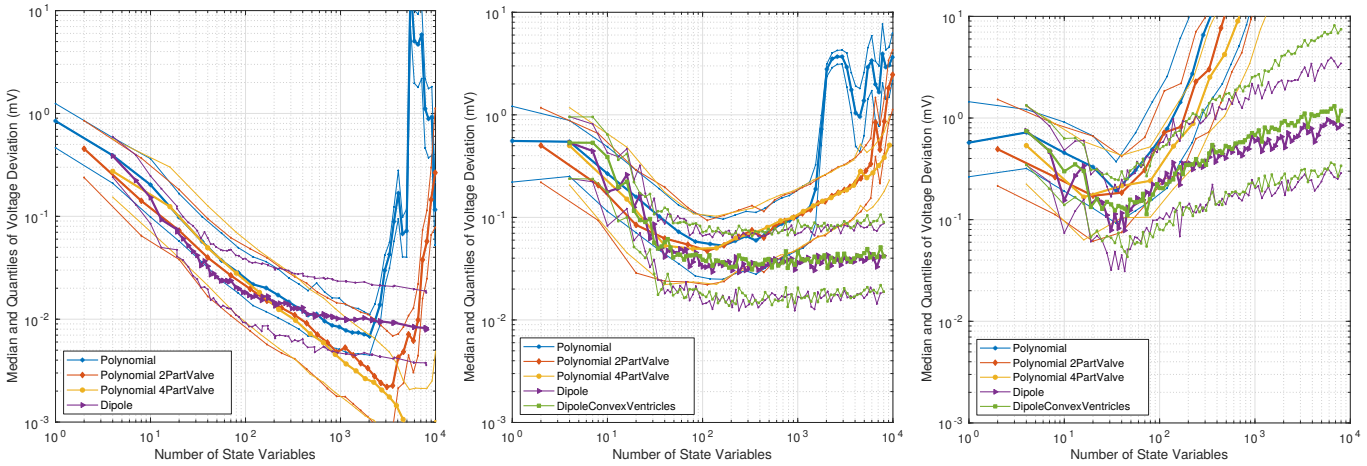

(a) SimA approximation, noise-free (b) SimB approximation (c) SimB extrapolation

Fig. 6. Approximation of the simulated VFF potential in the LA of SimA and SimB. The median error (p=0.5) is shown as thick line, and p=0.25 and p=0.75 as thin lines, plotted against the total number of parameters in the model, or their sum when multiple models were applied for different spatial regions (2PartValve, 4PartValve). The graphs show the worst results of all timesteps in (a), or the value at the R peak (164 ms) in (b, c). (a) All 9163 points in the LA cavity of SimA were used as training data. The estimation was validated in the 5 mm layer of the LA cavity near the endocardium. (b) All 37185 points in the LA cavity of SimB were used as training data, however corrupted with additive white Gaussian noise ($\sigma = 1\,\mathrm{mV}$). The estimation was evaluated in a 5 mm endocardial layer of the LA cavity. For example, the polynomial model in two partitions (red line) of 5th degree has $2 \cdot \frac{1}{6}(5+1)(5+2)(5+3) = 112$ degrees of freedom (3) and the median deviation between approximation and simulated VFF near the atrial endocardium is 0.0471 mV. In dipole models, the reference potential was estimated along with the dipole parameters as explained in (5). Dipoles were equally distributed into the ventricle's myocardium (Dipole), or into the convex hull of the ventricles (DipoleConvexVentricles). (c) A total of 11739 points further than 5 mm away from the endocardium inside the LA cavity of SimB were used as training data, corrupted with additive white Gaussian noise ($\sigma = 1\,\mathrm{mV}$). Estimator performance was evaluated using the remaining points close to the endocardium.

SimB was chosen for extrapolation assessment because the resolution of the mesh was equally high in the entire atrium. In contrast, the resolution of the geometrical mesh of SimA was very low inside the cavities with the resulting number of points (125 in LA cavity) turning out to be inadequate for model generation. Therefore, no extrapolation was attempted for this data set.

Table II also gives an overview of the median voltage deviation between simulated VFF and its approximation depending on the distance to the valve plane for one particular realization of the polynomial and dipole model in SimA and SimB, respectively. Data is again shown for the 5 mm blood layer adjacent to the atrial myocardium in the given distance to the valve plane $\pm 5\,\mathrm{mm}$. The VFF was approximated for SimA, and extrapolated for SimB. The particular models were chosen based on the performance shown in Fig. 6b as a trade-off between computational cost, model versatility, and the avoidance of overfitting effects for the polynomial models. They have a similar number of parameters for better comparison.

Fig. 7 shows the VFF suppression factor achieved by the dipole method. The potential distribution right at the endocardial surface was estimated after training the dipole model with electrical potentials from vertices inside the cavity with distances of more than 5 mm to the endocardium. A VFF suppression factor was calculated for each vertex as the quotient of the absolute value of the simulated ground truth voltage at the time of the R peak, and the deviation of the estimated voltage from the ground truth. See Supplemental Fig. 17 – 20 for the deviations in terms of voltage differences between ground truth and estimation for distinct dipole and polynomial methods applied to SimB.

In our in-silico geometric data sets SimA and SimB, exact information about atrial and ventricular tissue distribution was available and we could place the ventricular dipoles for the dipole method accordingly, i.e., equally distributed within the ventricular myocardium. However, in clinical data sets we have geometric information about the atrial endocardial surface only. Therefore, the question rose whether it is sufficient for the dipole method to place the ventricular dipoles merely into the rough position of the ventricles that can be inferred from the atrial geometry as in Fig. 2. In order to evaluate the sensitivity of the dipole method to the spatial dipole arrangement in silico, dipoles were placed within the ventricular myocardium of SimB and, for comparative purposes, also equally distributed within the convex hull of the ventricles. Fig. 6b and Fig. 6c show that there was no significant difference in approximation quality. As we do not aim at imaging the biological current sources [34] but exclusively at approximating the ventricular far field in the atria, it is sufficient to place dipoles in the vicinity of the real sources.

D. Clinical Application

Fig. 8 visualizes the performance of the proposed dipole method for the clinical data set. Details on the measured and estimated potential field within the atrial cavity are provided in Supplemental Fig. 12, 13, 16, and 22 as well as in the corresponding video supplement. The model was trained using the far field potential (Fig. 5) that was recorded during anatomy acquisition while pacing from the coronary sinus catheter. About one hour later, EGM data were acquired again during local high density mapping in AFib. Recorded uEGMs of eight channels are depicted in Fig. 8 (a). All channels show VFF

TABLE II
MEDIAN DEVIATION (mV) OF THE VFF APPROXIMATION WITHIN 1 cm SLICES PARALLEL TO THE VALVE PLANE. SIMA, WITHOUT NOISE; SIMB, WITH NOISE, $\sigma = 1\,\mathrm{mV}$. POLYNOMIAL MODEL, 5RD DEGREE WITH 2 PARTITIONS (112 PARAMETERS). DIPOLE MODEL, 42 DIPOLES (127 PARAMETERS)

	SimA		SimB	
Distance	Polynomial	Dipole	Polynomial	Dipole
0 cm	0.075	0.040	0.12	0.076
1 cm	0.041	0.027	0.056	0.045
2 cm	0.017	0.016	0.042	0.022
3 cm	0.0074	0.012	0.030	0.019
4 cm	0.0069	0.011	0.030	0.016
5 cm	0.0098	0.020	0.059	0.023

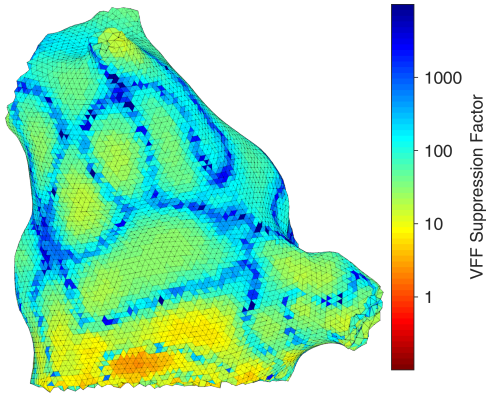

Fig. 7. The VFF approximation error was compared to the true value of the VFF for each location. The resulting suppression factor is depicted on a logarithmic color scale. A dipole model with 42 dipoles was trained with ventricular uEGMs and additive noise with $\sigma = 1\,\mathrm{mV}$ in the LA of SimB. Median suppression factor was 142 (IQR 65.2–322).

components simultaneous to the R peaks in the ECG. Standard filtering with high-pass and low-pass cutoff frequencies at 0.5 Hz and 300 Hz, respectively, did not eliminate the VFF components (b). Atrial activations, which were superimposed by the first VFF, can be identified and are in line with the timing of prior and subsequent activations after VFF removal with the dipole method on the raw uEGMs (c). Although a quantitative assessment is impossible due to the lack of ground truth data, the consistency within the acquired EGMs indicates successful VFF removal. Particularly in channel D2, the noise-floor becomes visible. Subsequent standard filtering helps to further improve signal quality (d).

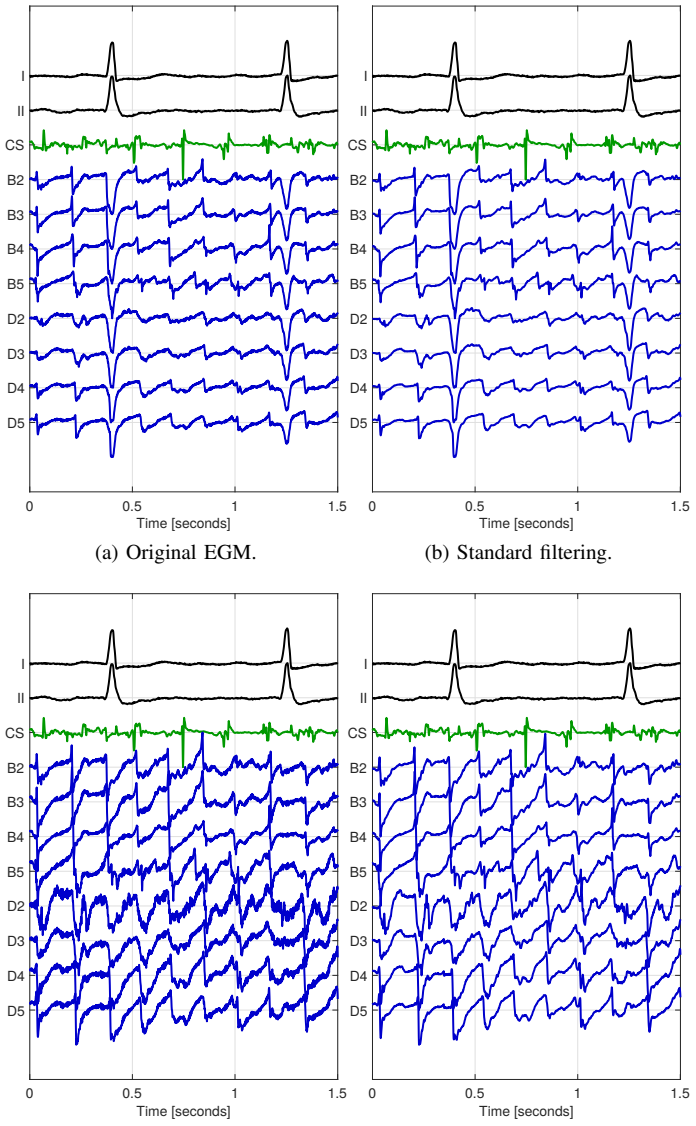

(a) Original EGM. (b) Standard filtering.

(c) After VFF removal. (d) After filtering.

Fig. 8. Example of clinical signals during AFib recorded 64 min after the initial anatomy and VFF data were acquired. Two ECG channels (black) are shown together with a bipolar channel of CS data (green). The recorded intracardiac uEGMs (blue) show noise and strong VFF components (a), which cannot be removed by standard high-pass/low-pass filtering (b). After applying the dipole model-based VFF removal, VFF components are notably less dominant (c). Additional high-pass/low-pass/notch filtering helps to further improve signal quality (d). All EGMs are normalized to the maximum absolute value for visualization.

IV. DISCUSSION

A. Main Findings

Three major findings can be derived from the study presented here. First, the VFF potential course is smooth in space exhibiting rather moderate spatial gradients, both in clinical and simulated data. This is in agreement with the current clinical practice to reduce the VFF component by subtracting two neighboring uEGMs yielding a bipolar signal. Second, mathematical models can represent the VFF distribution in the atria. We assessed both polynomial and dipole models, as both are capable of approximating and extrapolating data. Third, and most relevant for clinical translation, we showed that these models can be used to estimate and subsequently remove the VFF component in uEGMs during the clinical procedure even for varying atrial rhythms. The latter paves the way to exploit uEGMs during daily clinical practice as an alternative to the analysis of bEGMs, which strongly dominate the current state of the art.

B. Comparison of Methods

Both the polynomial and the dipole model were generally capable of approximating the VFF potential distribution. In most cases, the dipole model performed better than the polynomial model, especially for extrapolation and under

realistic noise conditions. This makes the dipole model stand out as the more favorable and robust choice. The number of dipoles could potentially be further reduced by reducing their density with increasing distance to the atria, i.e., towards the apex. Separating the spatial domain into distinct regions did improve the performance of the polynomial fit but had hardly any effect on the dipole model. This may indicate that the dipole approximation represents the physical reality more faithfully than the polynomial fit. However, the local polynomials covering regions distant from the ventricles performed better than dipole models when no noise was included, see Table II, SimA. This indicates that the assumption of an infinite homogeneous volume conductor, on which the dipole model is based, does not hold there.

During mapping with a 64-pole basket catheter, 64 data points can usually be acquired during each regular ventricular activation. Therefore, when assuming a heart rate of $70\,\mathrm{min}^{-1}$, the VFF is measured at up to 4480 points per minute. Based on the results shown in Fig. 6a and 6b, we deduce that about 10000 spatially distributed measurement points are sufficient to parametrize a suitable model with 42 dipoles to represent the VFF in the LA with a median deviation of about 0.03 mV under strong measurement noise. The initial map acquisition in standard atrial tachycardia electrophysiological studies takes about $15-20\,\mathrm{min}$ [3], [35], which gives ample time to acquire EGMs for the VFF model generation.

Model parametrization of a previously synchronized 20 min clinical data set could be performed in few seconds on a standard desktop machine (4 logical cores @3.2 GHz). 3.3 s were spent to generate and invert the lead field matrix for 100 dipoles and 95104 electrode positions. Parameter estimation and subsequent evaluation using a 262 ms QRS window at 953.674 Hz sampling rate took an additional 13 s for the 251 parameter vectors $\hat{\boldsymbol{c}}_k$ in total. Similarly, generation and inversion of Taylor polynomial matrices of 6th degree in 4 partitions (336 parameters) took 1.1 s. Estimation and evaluation for the 262 ms window took 5.4 s. After the model parameters $\hat{\boldsymbol{c}}_k$ are determined for each time step relative to the R peak, the model can be evaluated in real time, as soon as the R peak of the incoming ECG has been detected. The VFF-corrected uEGM can thus be visualized with a latency of less than $1\,\mathrm{s}$.

C. The Wilson Central Terminal as Reference Potential

Wilson central terminal (WCT) as a combination of limb ECG leads is commonly used as indifferent electrode for unipolar intracardiac measurements. From the early years on, however, using WCT has been critically discussed [36]. Data indicated that WCT is not truly zero if referenced to a point in infinity but varies during the cardiac cycle, being a potential source of misinterpretation of the readings when the explored signal is small [37]–[39]. Attempts have been made to re-reference unipolar recordings to an indifferent electrode in the inferior vena cava [2], which would presumably compensate the variation of WCT. A second component of the VFF, the electrical potential changes caused directly by ventricular activity in the atria, would however not be removed. Other groups generated an indifferent point, corresponding to infinity, using a shielded room [37], or applying numerical calculation of fields based on body surface potential maps [40], or by immersing the body into water [41]. They found that the Wilson central terminal does not represent an indifferent potential, but rather features a potential variation of about 0.3 mV depending on the individual patient. In some subjects, this can be a substantial part of the measured EGM.

From the perspective of a physicist, the indifferent point is arbitrary, as only potential *differences* occur in physical equations. It was claimed that the search for an indifferent reference in the human body was futile, as it does not exist [42]. However, physicists themselves also like to choose a reference point of the electrical potential that is most convenient for them, namely infinity. That way, the term corresponding to the reference point vanishes from the equations. Similarly, biomedical engineers try to find a way to present time courses of unipolar leads that are intuitive to interpret. The physician likes to have a unipolar plot whose morphology stems exclusively from cardiac activity local to the unipolar lead, without any superposed part that can be attributed to the reference potential. The latter would be considered an undesirable artifact. The importance of having plots without substantial components attributed to the reference potential is also emphasized by a survey among professional electrocardiologists, who revealed difficulties in grasping the meaning of the Wilson central terminal or its implication on the interpretation of ECGs [43]. The past has thus shown that pronouncing local atrial activity while suppressing field alterations caused by other sources such as the ventricles has been of high interest.

D. Comparison with Alternative Techniques

The most common approach to remove the VFF influence is to compute bEGMs. Considering the median gradient observed in our simulated and clinical data of about 0.1 mV/mm (Fig. 4) and an electrode spacing of 2.5 mm, the residual VFF can measure about 0.25 mV when the bipole is oriented along the maximum gradient and thus be considerably larger than the median residual VFF of 0.03 mV/mm obtained with our novel method. Although undesired common mode components are markedly reduced in bEGMs given a sufficient distance to the valve plane, the activity in the EGM can no longer be related to the one or the other electrode and compromises the spatial resolution. Even worse, the morphology of the bipolar signal depends on the orientation between the measuring catheter and the direction of the depolarization wave [4]. Maps based on shape or amplitude of bipolar signals, like low-voltage maps, are flawed when bipolar signals are used and impair the precision of any downstream method [2], [6].

Various signal processing techniques have been proposed to reject VFF, but they all require a training phase (5 s to 60 s) for each new catheter position. This would prolong mapping for state of the art point densities by more than one hour.

Our work can be best compared to the average beat subtraction approach. For the average beat subtraction approach, the following steps are required based on a mapping and a pacing catheter: 1) make sure patient is in sinus rhythm or produce a stable paced rhythm; 2) find R peaks in the ECG;

3) get pure VFF signals in time windows from the mapping catheter, aligned to R peak; 4) take the mean of VFF windows as the average beat; 5) by pacing, switch from SR to AFib or AFlut; 6) subtract the average VFF beat (aligned to the R peak) from 4) and use this as VFF-cleared uEGM; 7) move to new catheter position and start over from 1).

We propose to do steps 1) to 4) in parallel to initial anatomy acquisition for many different catheter positions. Based on accurate electrode tracking in modern electroanatomic mapping systems, we *recall* the appropriate interpolated average beat (the one from the same catheter position) later during ongoing atrial arrhythmia and subtract it from the uEGM. Furthermore, our spatial models exploit the smoothness and similarity of the VFF at adjacent atrial locations and facilitate approximation, interpolation, and limited extrapolation also under noise.

To validate this on clinical data, we simply plot the signals over time for comparison (Fig. 8; Supplemental Fig. 16). Some have also proposed to compare the spectra (i.e., the absolute value of Fourier transforms) in order to validate the performance of VFF cancellation methods [44], [45]. However, the Fourier phase is equally important for the shape of a signal. Thus, comparisons neglecting the phase are mere plausibility checks.

E. Limitations

The approaches presented in this study require to map the VFF component before being able to remove it. However, this does not prolong the mapping time as all necessary data are recorded during default anatomy acquisition. Data from the entire atrial chamber can only be used for training the VFF model if atrial and ventricular activity can be separated in time domain (i.e., ventricular activation takes place after the atria are depolarized completely, like in sinus rhythm). If the patient cannot be cardioverted to sinus rhythm and mapping is performed during AFib or AFlut, temporal separation may not be possible. In this case, only data recorded at positions with sufficient distance to the endocardial wall may be usable for model generation and the capability of the method to spatially extrapolate the field distribution becomes relevant. Our method requires the ventricular depolarization pattern to be always of the same type; it cannot remove VFF from sporadic ventricular ectopic beats. We also rely on sufficient navigational accuracy. Electrode localization errors entail evaluating the generated VFF model at an inaccurate position and thus flaw the result.

F. Outlook

Even if the ventricular depolarization pattern is generally stable, there are slight morphological variances of the QRS complex due to e.g. breathing [46] or fluctuations in mental stress level [47], which can be detected from ECG [20], [7]. If for example the temporal width of the proposed spatio-temporal VFF model is adapted on-line according to the instantaneous QRS width from ECG, or by directly using heart phase estimation [48] instead of QRS detection, VFF cancellation can potentially be further improved. For smooth visualization, the VFF window could be modeled with a continuous transition instead of a rectangular function.

Instead of the infinite homogeneous conductor assumption, a dipole model for the specific atrial surface mesh could be derived based on numerical field calculation, e.g., the boundary element method. Also, dipole placement might be optimized in such a way that even when atrial activity would be present during anatomy acquisition, the model would only adopt the ventricular part. For example, it might help not to place any dipoles too close to the atria.

V. Conclusion

The VFF poses a major challenge to the interpretation of uEGMs. Existing methods for VFF removal are based on statistical assessment of the local EGM, requiring several seconds of data acquired at each position and are thus hardly applicable in clinical practice. We successfully modeled the spatio-temporal course of the VFF potential in the atria in a patient-specific manner, allowing to estimate it at each position and timepoint. Both clinical and simulated data confirmed that spatial VFF models can cancel the ventricular component from atrial measurements reliably and effectively. Using our novel method, a clear and continuous uEGM is obtained that exhibits almost only local atrial activity. As opposed to bEGMs, the atrial activity in the VFF-cleared uEGM signal remains local to one electrode. In addition, the amplitude and morphology of the resulting uEGM is independent from the relative orientation of catheter electrodes and wavefront direction. Our novel method can easily be incorporated into modern electroanatomic mapping systems without prolonging the intervention. The resulting high-quality uEGMs are advantageous for activation time assignment as required for local activation time and conduction velocity mapping [49] and they are vital for substrate mapping. As this method allows to leverage the full potential of uEGMs, it can potentially contribute to the quality of ablation procedures and increase the currently sub-optimal long-term success rates.

Supplementary Material

Our online supplemental material comprises details on the model generation, simulated activation patterns, and clinical data processing. Moreover, additional results regarding the field distribution (including two movies) and VFF estimation are presented.

Acknowledgment

The authors would like to thank Annika Haas from Boston Scientific for technical support during data acquisition and Robin Moss from Universitäts-Herzzentrum Freiburg • Bad Krozingen GmbH for the mesh of SimB.

References

[1] T. Oesterlein, *et al.*, "Method and system for determining ventricular far field contribution in atrial electrograms," EP/US Patent EP3 446 628A1, US20 190 059 765A1, Aug. 24, 2017.

[2] U. B. Tedrow and W. G. Stevenson, "Recording and interpreting unipolar electrograms to guide catheter ablation," *Heart Rhythm Journal*, vol. 8, no. 5, pp. 791–796, 2011.

[3] M. Takigawa, *et al.*, "Revisiting anatomic macroreentrant tachycardia after atrial fibrillation ablation using ultrahigh-resolution mapping: Implications for ablation." *Heart Rhythm Journal*, vol. 15, no. 3, pp. 326–333, 2018.

[4] S. Schuler, *et al.*, "Influence of catheter orientation, tissue thickness and conduction velocity on the intracardiac electrogram," in *Biomedical Engineering / Biomedizinische Technik*, vol. 58, no. s1, 2013.

[5] K. Otomo, *et al.*, "Local unipolar and bipolar electrogram criteria for evaluating the transmurality of atrial ablation lesions at different catheter orientations relative to the endocardial surface," *Heart Rhythm Journal*, vol. 7, no. 9, pp. 1291–1300, 2010.

[6] G. Ndrepepa, *et al.*, "Activation time determination by high-resolution unipolar and bipolar extracellular electrograms in the canine heart," *Journal of Cardiovascular Electrophysiology*, vol. 6, no. 3, pp. 174–188, 1995.

[7] G. Lenis, *et al.*, "P wave detection and delineation in the ECG based on the phase free stationary wavelet transform and using intracardiac atrial electrograms as reference," *Biomedical Engineering / Biomedizinische Technik*, vol. 61, no. 1, pp. 37–56, 2016.

[8] ——, "Comparison of baseline wander removal techniques considering the preservation of st changes in the ischemic ecg: A simulation study," *Computational and Mathematical Methods in Medicine*, vol. 2017, no. Article ID 9295029, p. 13, 2017.

[9] S. Huck, *et al.*, "Preprocessing of unipolar signals acquired by a novel intracardiac mapping system," in *Current Directions in Biomedical Engineering*, vol. 2, no. 1. De Gruyter, 2016, pp. 259–262.

[10] J. J. Rieta and F. Hornero, "Comparative study of methods for ventricular activity cancellation in atrial electrograms of atrial fibrillation," *Physiological Measurement*, vol. 28, no. 8, pp. 925–936, 1 2007.

[11] J. L. Salinet Jr., *et al.*, "Analysis of QRS-T subtraction in unipolar atrial fibrillation electrograms," *Medical & Biological Engineering & Computing*, vol. 51, no. 12, pp. 1381–1391, Dec 2013.

[12] E. B. Caref, *et al.*, "Improved activation time assignment of unipolar electrograms from ischemic canine epicardium," *Pacing and Clinical Electrophysiology: PACE*, vol. 34, no. 9, pp. 1105–1115, 2011.

[13] J. Slocum, *et al.*, "Computer detection of atrioventricular dissociation from surface electrocardiograms during wide QRS complex tachycardias." *Circulation*, vol. 72, no. 5, pp. 1028–1036, 1985.

[14] M. Stridh and L. Sornmo, "Spatiotemporal QRST cancellation techniques for analysis of atrial fibrillation," *IEEE Transactions on Biomedical Engineering*, vol. 48, no. 1, pp. 105–111, Jan 2001.

[15] F. Castells, *et al.*, "Principal component analysis in ECG signal processing," *EURASIP Journal on Advances in Signal Processing*, vol. 2007, no. 1, p. 98, 2007.

[16] C. Schilling, *et al.*, "PCA-based ventricular far field cancellation in intraatrial electrograms," in *Biomedical Engineering / Biomedizinische Technik*, vol. 55, no. s1. Walter de Gruyter, 2010, pp. 49–52.

[17] T. G. Oesterlein, *et al.*, "Removing ventricular far-field signals in intracardiac electrograms during stable atrial tachycardia using the periodic component analysis," *Journal of Electrocardiology*, vol. 48, no. 2, pp. 171–180, 2015.

[18] G. Seemann, *et al.*, *Framework for Modular, Flexible and Efficient Solving the Cardiac Bidomain Equations Using PETSc*. Berlin, Heidelberg: Springer Berlin Heidelberg, 2010, pp. 363–369.

[19] O. Dössel, "Inverse problem of electro- and magnetocardiography: Review and recent progress," *International Journal of Bioelectromagnetism*, vol. 2, no. 2, 2000.

[20] G. Lenis, T. Baas, and O. Dössel, "Ectopic beats and their influence on the morphology of subsequent waves in the electrocardiogram," *Biomedical Engineering / Biomedizinische Technik*, vol. 58, no. 2, pp. 109–119, 2013.

[21] M. Alessandrini, *et al.*, "A computational framework to benchmark basket catheter guided ablation in atrial fibrillation," *Frontiers in Physiology*, vol. 9, p. 1251, 1 2018.

[22] T. Oesterlein, *et al.*, "Basket-type catheters: Diagnostic pitfalls caused by deformation and limited coverage," *BioMed Research International*, pp. 1–13, 1 2016.

[23] V. Spitzer, *et al.*, "The visible human male: A technical report," *Journal of the American Medical Informatics Association*, vol. 3, no. 2, pp. 118–130, 1996.

[24] A. Loewe, *et al.*, "ECG-based detection of early myocardial ischemia in a computational model: Impact of additional electrodes, optimal placement, and a new feature for ST deviation," *BioMed Research International*, vol. 2015, p. 530352, 2014.

[25] ——, "Influence of the earliest right atrial activation site and its proximity to interatrial connections on P-wave morphology," *EP – Europace – European Journal of Pacing, Arrhythmias and Cardiac Electrophysiology*, vol. 18, no. S4, pp. iv35–iv43, 2016.

[26] J. D. Bayer, *et al.*, "A novel rule-based algorithm for assigning myocardial fiber orientation to computational heart models," *Annals of Biomedical Engineering*, vol. 40, no. 10, pp. 2243–2254, 2012.

[27] A. Wachter, *et al.*, "Mesh structure-independent modeling of patient-specific atrial fiber orientation," in *Current Directions in Biomedical Engineering*, vol. 1, no. 1. De Gruyter, 2015, pp. 409–412.

[28] M. Courtemanche, R. J. Ramirez, and S. Nattel, "Ionic mechanisms underlying human atrial action potential properties: Insights from a mathematical model," *American Journal of Physiology – Heart and Circulatory Physiology*, vol. 275, no. 1 Pt 2, pp. H301–H321, 1998.

[29] A. Loewe, *et al.*, "Left and right atrial contribution to the P-wave in realistic computational models," in *Functional Imaging and Modeling of the Heart 2015, LNCS*, no. 9126, 2015, pp. 439–447.

[30] W. Kahlmann, *et al.*, "Modelling of patient-specific Purkinje activation based on measured ECGs," in *Current Directions in Biomedical Engineering*, vol. 3, no. 2. de Gruyter, 2017, pp. 171–174.

[31] K. H. W. J. ten Tusscher and A. V. Panfilov, "Alternans and spiral breakup in a human ventricular tissue model," *American Journal of Physiology – Heart and Circulatory Physiology*, vol. 291, no. 3, pp. H1088–100, 2006.

[32] S. A. Niederer, *et al.*, "Verification of cardiac tissue electrophysiology simulators using an N-version benchmark," *Philosophical Transactions of the Royal Society A: Mathematical, Physical and Engineering Sciences*, vol. 369, no. 1954, pp. 4331–4351, 2011.

[33] L. A. Unger, *et al.*, "Noise quantification and noise reduction for unipolar and bipolar electrograms," in *Computing in Cardiology*, 2019.

[34] M. Cluitmans, *et al.*, "Validation and opportunities of electrocardiographic imaging: From technical achievements to clinical applications," *Frontiers in physiology*, vol. 9, no. 1305, 2018.

[35] D. G. Latcu, *et al.*, "Selection of critical isthmus in scar-related atrial tachycardia using a new automated ultrahigh resolution mapping system," *Circulation: Arrhythmia and Electrophysiology*, vol. 10, no. 1, 1 2017.

[36] E. Frank, "General theory of heart-vector projection," *Circulation Research*, vol. 2, no. 3, pp. 258–270, may 1954.

[37] G. E. Dower, J. A. Osborne, and A. D. Moore, "Measurement of the error in Wilson's central terminal: an accurate definition of unipolar leads," *British Heart Journal*, vol. 21, pp. 352–360, July 1959.

[38] J. E. Madias, "On recording the unipolar ECG limb leads via the Wilson's vs the Goldberger's terminals: aVR, aVL, and aVF revisited." *Indian Pacing and Electrophysiology Journal*, vol. 8, pp. 292–297, 2008.

[39] G. D. Gargiulo, "True unipolar ECG machine for Wilson central terminal measurements," *BioMed Research International*, vol. 2015, p. 586397, 2015.

[40] N. Miyamoto, *et al.*, "The absolute voltage and the lead vector of Wilson's central terminal." *Japanese Heart Journal*, vol. 37, pp. 203–214, Mar. 1996.

[41] F. N. Wilson, *et al.*, "On Einthoven's triangle, the theory of unipolar electrocardiographic leads, and the interpretation of the precordial electrocardiogram," *American Heart Journal*, vol. 32, no. 3, pp. 277–310, Sept. 1946.

[42] H. Burger, "The zero of potential: A persistent error," *American Heart Journal*, vol. 49, no. 4, pp. 581–586, apr 1955.

[43] L. Bacharova, *et al.*, "Where is the central terminal located? In search of understanding the use of the wilson central terminal for production of 9 of the standard 12 electrocardiogram leads," *Journal of Electrocardiology*, vol. 38, no. 2, pp. 119–127, 2005.

[44] Q. Xi, A. V. Sahakian, and S. Swiryn, "The influence of QRS cancellation on signal characteristics of atrial fibrillation in the surface electrocardiogram," in *Computers in Cardiology*, Sep. 2002, pp. 13–16.

[45] Q. Xi, A. V. Sahakian, and S. Swiryn, "The effect of QRS cancellation on atrial fibrillatory wave signal characteristics in the surface electrocardiogram," *Journal of Electrocardiology*, vol. 36, no. 3, pp. 243 – 249, 2003.

[46] G. Lenis, F. Conz, and O. Dössel, "Combining different ECG derived respiration tracking methods to create an optimal reconstruction of the breathing pattern," in *Current Directions in Biomedical Engineering*, vol. 1, no. 1. September 16-18, Lübeck: Jahrestagung der DGBMT - Deutschen Gesellschaft für Biomedizinische Technik im VDE, 2015, pp. 54–57.

[47] G. Lenis, *et al.*, "Electrocardiographic features for the measurement of drivers' mental workload," *Applied Ergonomics*, vol. 61, no. May, pp. 31–43, 2017.

[48] G. Kurz and U. D. Hanebeck, "Heart phase estimation using directional statistics for robotic beating heart surgery," in *Proceedings of the 18th International Conference on Information Fusion (Fusion 2015)*, Washington D.C., USA, July 2015.

[49] B. Verma, *et al.*, "Regional conduction velocity calculation from clinical multichannel electrograms in human atria," *Computers in Biology and Medicine*, vol. 92, pp. 188–196, 1 2018.